Zinc Induces Structural Reorganization of Gelatin Binding Domain from Human Fibronectin and Affects Collagen Binding

ARTICLE *in* STRUCTURE · JUNE 2010

Impact Factor: 5.62 · DOI: 10.1016/j.str.2010.03.012 · Source: PubMed

5 AUTHORS, INCLUDING:

Marc Graille
École Polytechnique
76 PUBLICATIONS **1,674** CITATIONS
SEE PROFILE

Michele Reboud-Ravaux
Pierre and Marie Curie University - Paris 6
98 PUBLICATIONS **1,526** CITATIONS
SEE PROFILE

Structure
Article

Zinc Induces Structural Reorganization of Gelatin Binding Domain from Human Fibronectin and Affects Collagen Binding

Marc Graille,[1,*] Maurice Pagano,[2] Thierry Rose,[3] Michèle Reboud Ravaux,[2] and Herman van Tilbeurgh[1,*]
[1]IBBMC, Université Paris 11, IFR115, CNRS UMR8619, Orsay Cedex F-91405, France
[2]Enzymologie Moléculaire et Fonctionnelle, Case 256, UR 4, UPMC-Paris Universitas, Paris Cedex 05, F-75252, France
[3]PFBMI, Département de Biologie Structurale et Chimie, Institut Pasteur, Paris Cedex 15, F-75724, France
*Correspondence: marc.graille@u-psud.fr (M.G.), herman.van-tilbeurgh@u-psud.fr (H.v.T.)
DOI 10.1016/j.str.2010.03.012

SUMMARY

Fibronectin is a modular extracellular matrix protein involved in cell adhesion, cell motility, wound healing, and maintenance of cell morphology. It is composed of multiple repeats of three distinct modules: F_I, F_{II}, and F_{III}. Various combinations of these modules create fragments able to interact with different constituents of the extracellular matrix. Here, we present the 2.5-Å resolution crystal structure of its 45-kDa gelatin-binding domain (GBD; $6F_I$-$1F_{II}$-$2F_{II}$-$7F_I$-$8F_I$-$9F_I$), which also corresponds to the C-terminal half of the migration stimulating factor, a Fn splice variant expressed in human breast cancers. GBD forms a very compact zinc-mediated homodimer, in stark contrast with previous structures of fibronectin fragments. Most remarkably, $8F_I$ no longer adopts the canonical F_I fold but is composed of two long strands that associate with $7F_I$ and $9F_I$ into a large β-sheet superdomain. Binding studies in solution confirmed that Zn induces conformational rearrangements and causes loss of binding of Fn-GBD to high-affinity collagen peptides. These data suggest the Zn may play a regulatory role for the cellular functions of fibronectin.

INTRODUCTION

Fibronectin (Fn) is a large and flexible multifunctional glycoprotein and a prominent component of the extracellular matrix (ECM). Fn is also found at high concentrations in plasma. Through its ability to interact with several distinct partners (collagen, heparin, fibrin, and cell-surface receptors of the integrin family), Fn plays key roles in cell adhesion, cell morphology, wound healing, cell migration, and embryogenic differentiation (Hynes, 1990; Pankov and Yamada, 2002). As part of the ECM, Fn forms a fibrillar network (Morla et al., 1994), and in blood plasma, it exists as a dimer of two similar but not identical polypeptide chains of 220–250 kDa each, connected by two disulfide bridges at the C terminus of the protein. In humans, alternative splicing of Fn mRNA leads to the expression of a 77-kDa protein also known as migration stimulating factor (MSF) that corresponds to the N-terminal part (Liu et al., 2003; Schor et al., 2003). This soluble protein is secreted by fibroblasts in fetal skin and breast cancer, and stimulates fibroblast migration (Schor et al., 1988).

Fn has a modular architecture made by a combination of three structurally distinct modules called F_I, F_{II}, and F_{III} (Figure 1A) (for reviews, see Chothia and Jones, 1997; Erickson et al., 1981; Erickson and Carrell, 1983; Potts and Campbell, 1996). Upon limited proteolytic digestion of Fn, several functional fragments with specific ligand-binding properties can be isolated (Figure 1A) (Hynes, 1990). The 3D structures of fragments $1F_I$-$2F_I$, $2F_I$-$3F_I$, $4F_I$-$5F_I$, $6F_I$-$1F_{II}$, $8F_I$-$9F_I$, $7F_{III}$-$8F_{III}$-$9F_{III}$-$10F_{III}$, and $12F_{III}$-$13F_{III}$-$14F_{III}$ have revealed that these contiguous modules are arranged as extended arrays, supporting the "string of beads" as a model for the structural organization of Fn (Bocquier et al., 1999; Erat et al., 2009; Leahy et al., 1996; Potts et al., 1999; Rudiño-Piñera et al., 2007; Sharma et al., 1999; Williams et al., 1994). Extensive intermodule interactions were, however, observed between $6F_I$ and $2F_{II}$ domains using thermodynamic studies and in the NMR structure of the $6F_I$-$1F_{II}$-$2F_{II}$ fragment of the Fn gelatin-binding domain (GBD) (Litvinovich et al., 1991; Pickford et al., 2001) as well as between $1F_{III}$-$2F_{III}$ and the N-terminal 30-kDa heparin-binding fragment (Vakonakis et al., 2007).

Fn and integrin receptors play an essential role in the formation of collagen fibers in cell cultures. It is known that Fn interacts with collagen in this process. The collagen-binding site on fibronectin was shown to reside in a fragment composed of $6F_I$-$1F_{II}$-$2F_{II}$-$7F_I$-$8F_I$-$9F_I$ and is known GBD. The majority of Fn collagen interaction studies in vitro used either denatured collagen (gelatin) or small collagen I fragments (Engvall and Ruoslahti, 1977; Erat et al., 2009; Ingham et al., 1988, 2002). GBD binds strongly to gelatin columns and can only be eluted at high urea concentrations. Anti-GBD antibodies inhibit collagen fiber formation in fibroblasts (McDonald et al., 1982). Collagenase cleavage sites in collagen I form the cognate Fn interaction sites (Kleinman et al., 1978). Peptide scanning using NMR and fluorescence recently identified collagen peptides that bind to two different Fn-GBD fragments (8–$9F_I$ and $6F_I$-$1F_{II}$-$2F_{II}$-$7F_I$) (Erat et al., 2009). The identified peptide spanning residues G778–G799 is situated at the C-terminal of the matrix metalloproteinase I cleavage site. The crystal structure of this peptide in complex with 8-$9F_I$ showed that the collagen peptide adopts an elongated strand conformation, antiparallel to the $8F_I$ E-strand (Erat et al., 2009).

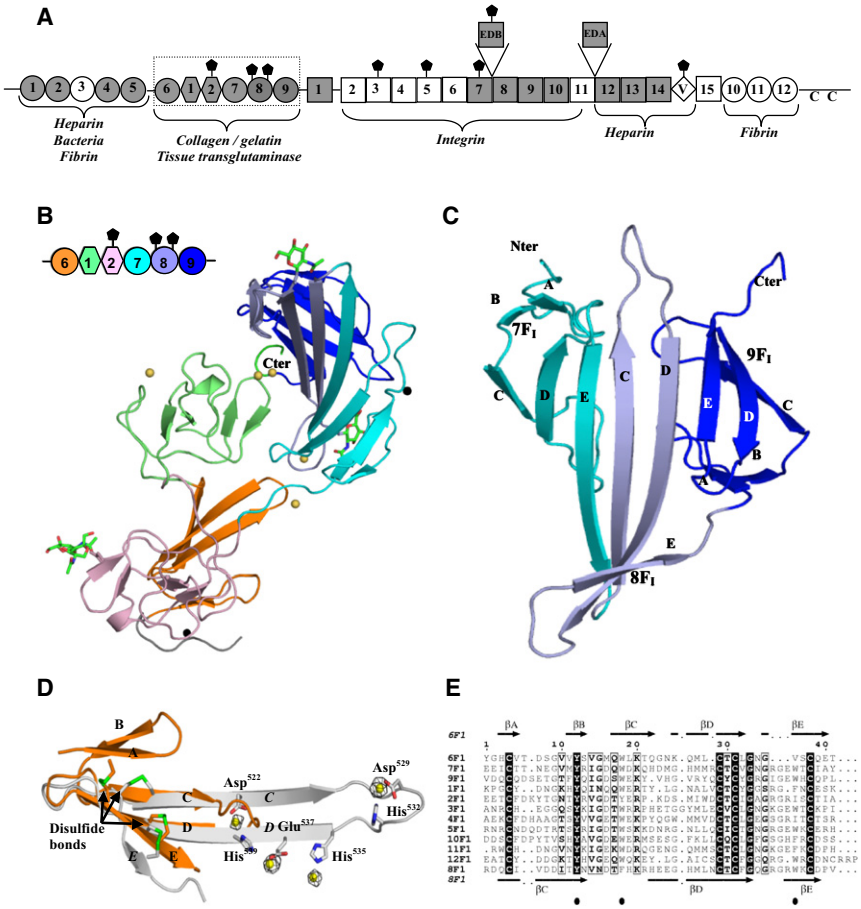

Figure 1. Ribbon Representation of the GDB

(A) Schematic representation of human Fn. Modules whose structures have been solved are in gray. Glycosylation sites are depicted by closed diamonds. Interacting partners for the different Fn fragments are indicated. The letter *C* represents cysteinyl residues involved in intermolecular disulfide bridges. The fragment described in this study is boxed.

(B) Ribbon representation of the GBD monomer. The schematic representation on the top left represents the color code used for each module in all figures. Zn^{2+} ions present at crystal contacts or at the GBD dimer interface are depicted as black and yellow spheres, respectively. Sugars are shown in sticks.

(C) Representation of the large C-terminal domain.

(D) Superimposition of $8F_I$ as observed in the crystal structure of the complex with collagen peptide (orange) onto our $8F_I$ (gray). Disulfide bridges are shown as sticks. Amino acids from $8F_I$ that are responsible for zinc binding are shown as sticks. Zn^{2+} ions are depicted as yellow spheres. Anomalous map (black) contoured at 9σ is shown around the Zn^{2+} ions.

(E) Sequence alignment of the 12 F_Is from human Fn. Secondary structure elements for all F_I modules are on top, except for those of our X-ray $8F_I$ structure, which are at the bottom. Strictly conserved residues are in white on a black background. Well-conserved amino acids are boxed. Black circles below the alignment indicate positions contributing to the formation of the hydrophobic core of classical F_I modules.

Although a few structures of single domains or domain combinations of Fn are known, structural information is missing for many complete functional fragments. We have solved the crystal structure of the Fn GBD fragment. This 45-kDa acidic GBD is obtained by cathepsin D and tryptic digestion of Fn from human plasma and corresponds to the C-terminal half of the MSF. It consists of $6F_I$-$1F_{II}$-$2F_{II}$-$7F_I$-$8F_I$-$9F_I$ and carries N-glycosylations on three Asn residues (Asn^{430} from $2F_{II}$ and Asn^{528} and Asn^{542} from $8F_I$ that account for 5–10 kDa (Ingham et al., 1989, 1995). Surprisingly, Fn forms a very compact Zn-induced dimeric structure.

RESULTS

Fn Gelatin-Binding Domain Forms a Compact Structure

Crystals of Fn-GBD could only be obtained in the presence of 30–50 mM $ZnSO_4$ from 100 nl crystallization drops. The structure has been solved using the single-wavelength anomalous diffraction (SAD) method exploiting the anomalous scattering from bound Zn^{2+} ions and was refined to 2.5 Å resolution (Table 1). The final model contains all the residues from Gln^{297} to Thr^{604} as well as seven zinc atoms. The crystal asymmetric unit contains one copy of GBD. GBD adopts a curved elongated shape with approximate dimensions 40 × 40 × 82 $Å^3$. Overall, the structure of GBD is different from what was expected and cannot be described as a simple multimodular chain of well-documented F_I and F_{II} domains. GBD consists of three layers (Figure 1B): a N-terminal lobe made by the association of $6F_I$ (Gly^{306}-Thr^{345}) and $2F_{II}$ (His^{404}-Met^{463}), the central $1F_{II}$ (Ala^{346}-Asp^{403}), and a large C-terminal lobe (Ala^{464}-Thr^{604}, $7F_I$-$8F_I$-$9F_I$). A previous NMR structure of the $6F_I$-$1F_{II}$-$2F_{II}$ fragment showed that $6F_I$ and $2F_{II}$ tightly pack, burying 800 $Å^2$ of hydrophobic solvent accessible surface area (ASA) (Pickford et al., 2001). Buried surface areas were calculated as follows: ASA molA + ASA molB − ASA molAB. The NMR and present crystal structures of the $6F_I$-$2F_{II}$ pair are in excellent agreement (rmsd of 1.4 Å over 90 Cα atoms from $6F_I$ and $2F_{II}$). The relative orientation and position of $1F_{II}$ relative to $6F_I$-$2F_{II}$ were ill defined in the solution structure. In the present crystal structure, $1F_{II}$ (rmsd is 1.3 Å over 49 Cα atoms compared with its NMR structure) is sandwiched between the N- and C-terminal lobes (1,025 $Å^2$ and 850 $Å^2$ buried surface area, respectively) and contributes considerably to dimer formation (see further). Also the C-terminal lobe is organized as a compact structure. Most remarkably, the three C-terminal F_Is ($7F_I$, $8F_I$, and $9F_I$) can no longer be considered as individual modules but are organized into a single superdomain consisting of an eight-stranded antiparallel β-sheet (Figure 1C). The classical F_I fold, as represented by $7F_I$, consists of a short β-hairpin (strands A and B) that packs against a three-stranded (strands C, D, and E) antiparallel β-sheet (Baron et al., 1990). A disulfide bond connects both sheets. Modules $7F_I$ (Ala^{464}-Arg^{515}) and $9F_I$ (Asp^{559}-Thr^{604}) adopt this fold (rmsd value

Table 1. Data Collection Statistics

	Native	SAD
Data collection		
Resolution (Å)	20.0–2.4 (2.53–2.4)	50.0–3.0 (3.16–3.0)
Space group	P 3_221	P 3_221
Unit cell parameters	a = b = 124.8 Å; c = 60.6 Å	a = b = 125.2 Å; c = 60.9 Å
Total no. reflections	46,596	130,597
Total no. unique reflections	20,851	11,280
R_{sym} (%)[a]	8.4 (62.1)	13.7 (48.4)
Completeness (%)	97.3 (96.6)	100 (100)
I/σ (I)	9 (1.2)	18.6 (4.1)
Redundancy	2.2 (2.1)	11.6 (11.8)
Refinement		
Resolution (Å)	20–2.5	
R/R_{free} (%)[b]	19.4 / 21.9	
Rmsd bonds (Å)	0.010	
Rmsd angles (°)	1.22	
B Wilson (Å^2)	58	
Mean B factor (Å^2) protein/ water/zinc/ glycosylation	71/54/63/103	
Ramachandran plot		
Most favored	90.6%	
Allowed	9.4%	

[a] $R_{sym} = \Sigma_h\Sigma_i|I_{hi} - < I_h >|/\Sigma_h\Sigma_i I_{hi}$, where I_{hi} is the *i*th observation of the reflection h, and $< I_h >$ is the mean intensity of reflection h.
[b] $R_{factor} = \Sigma\ ||F_o| - |F_c|| / |F_o|$. R_{free} was calculated with a small fraction (5%) of randomly selected reflections.

between our $7F_I$ and the NMR $7F_I$ structure is 1.4 Å over 40 Cα atoms, and rmsd between our $9F_I$ and the X-ray structure of $9F_I$ obtained in the presence of collagen peptide is 0.6 Å over 46 Cα atoms). Their β-hairpins (βA and βB) occupy opposite positions on the convex face of the main β-sheet of the C-terminal lobe (Figure 1C). The Fn-GBD structure is the first example of a fragment containing three contiguous F_Is. Previous structures of F_I pairs had revealed an organization as "module arrays" with no or minor contacts between F_Is (Bocquier et al., 1999; Potts et al., 1999; Rudiño-Piñera et al., 2007; Williams et al., 1994). In contrast with available structural information on F_Is, $8F_I$ does not adopt a canonical F_I fold in our structure but consists of a three-stranded β sheet. We labeled the three strands of the new $8F_I$ fold as C, D, and E. To visualize the structural differences with a classical F_I fold, we superposed $8F_I$ from our crystal structure with that from the recently published $8F_I$-$9F_I$ fragment in complex with a collagen peptide (Erat et al., 2009) (Figure 1D). In this complex, $8F_I$ and $9F_I$ domains adopt a canonical F_I fold and are arranged linearly, making few interdomain contacts. In our structure, the $8F_I$ is completely rearranged. As a consequence, the small two-stranded β-sheet made by strands A and B is absorbed in a new, long β-strand (strand C) (Figure 1E). Residues 530–534 that were part of the former C-strand now form the loop connecting strands C and D. The linker (residues 533–538) that connects the strands C and D in the classical F_I now corresponds to the N-terminal part of the much longer strand D. Both structures of classical and rearranged $8F_I$ can only be superposed on parts of their C, D, and E strands (Figures 1D and 1E). The three aromatic residues that form the hydrophobic core in a classical F_I context (Tyr^{525}, Phe^{531}, and Trp^{553}) are not clustered in the present $8F_I$ structure. Tyr^{525} is part of the C-ter lobe hydrophobic core but Phe^{531} and Trp^{553} are interacting with $6F_I$ from the same protomer and $1F_{II}$ from the second protomer of the homodimer (see further), respectively. Strand E from $7F_I$ is four residues longer than usual for a canonical F_I. The linker connecting $7F_I$ to $8F_I$ contributes these extra strand residues. In fact, in Zn-GBD the 7, 8, and $9F_I$s do not fold into individual modules but are associated into a single superdomain. This domain is formed by a large eight-stranded antiparallel β-sheet (grouping strands C, D, and E from each F_I). The $8F_I$ domain contains two disulfide bonds: Cys^{518}-Cys^{545} (connecting stands A and D) and Cys^{543}-Cys^{555} (connecting strands D and E). In our present structure, these disulfide bonds are maintained. Upon superposition of the two $8F_I$ structures (Figure 1D), the Cys^{543}-Cys^{555} disulfide bonds almost overlap, whereas the Cys^{518}-Cys^{545} disulfide bond pivots over 180° following the rearrangement of the strands.

Structure of Fn-GBD Reveals Multiple Zn-Binding Sites

Crystals of Fn-GBD were only obtained in the presence of Zn. We therefore collected diffraction data at the anomalous Zn edge wavelength and seven Zn atoms per monomer could be unambiguously positioned in the crystal structure. These Zn atoms create complex interaction networks between the different modules but also between subunits of the Fn-GBD dimer (see further). Four of these sites involve residues from the $8F_I$ (Figure 1D). One of these Zn sites bridges strands C and D (Asp522/His539) (see Figure S2C available online). Two other Zn coordinate side chains from the strand D (His535 and Glu537). Residues from the linker between strands C and D (Asp529 and His 532) (Figure S2D) coordinate the fourth Zn. These Zn sites are very likely to be responsible for the drastic rearrangement of $8F_I$. Comparison with the structure $8F_I$-$9F_I$ in complex with a collagen fragment (Erat et al., 2009) shows that none of these Zn sites could exist in the context of a canonical $8F_I$ fold. Five of seven Zn sites coordinate residues from different Fn modules and probably are important for the observed compaction of Fn-GBD. Most of the Zn sites involve both histidine and aspartate/glutamate ligands (Figures S1 and S2), and some of them are very similar to active site Zn ion environments of metalloproteases such as carboxypeptidase and thermolysin.

Homodimerization and Zn^{2+} Binding

Although only one copy of Fn-GBD is present in the asymmetric unit, an extensive Fn-GBD homodimer, burying 4,500 Å^2 solvent ASA, can be generated by a crystallographic twofold symmetry operation. This buried surface area is much larger than any of the other Zn-mediated crystal contacts (<1,000 Å^2). The two GBD monomers are associated in parallel, creating two important interaction surfaces (Figures 2A and 2B). The first involves the $2F_{II}$ modules (buried ASA of 1,200 Å^2) (Figure S3A) and in the second, $1F_{II}$ is packed against the concave face of the β-sheet from the C-ter lobe (buried ASA of 1,300 Å^2) (Figure S3C). Homodimerization further involves interactions between $2F_{II}$ and the large C-ter lobe (buried ASA of 500 Å^2) (Figure S3B). A total of 64 monomer residues and 18 hydrogen bonds contribute to

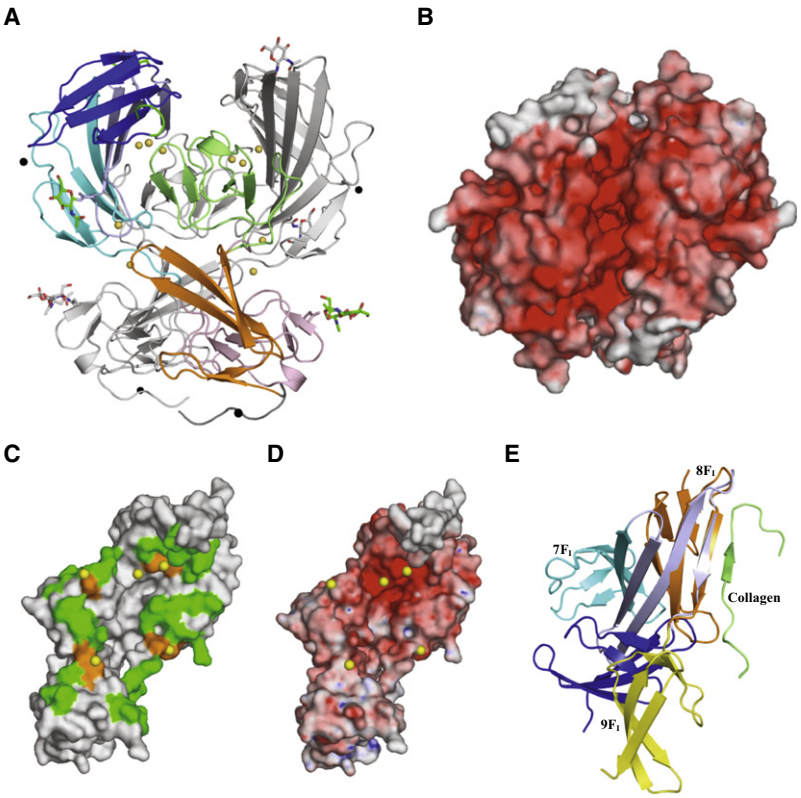

Figure 2. Surface Representation of GBD

(A) Ribbon representation of the homodimer. One monomer is colored as in Figure 1B; the other is in gray.

(B) Surface representation of the electrostatic potential, calculated in absence of zinc, for the GBD homodimer. Regions of the surface with negative or positive potentials are colored red and blue, respectively.

(C) Surface mapping of residues involved in homodimer formation (green). Dimer amino acids coordinating Zn^{2+} ions (yellow spheres) are in orange.

(D) Surface representation of the electrostatic potential, calculated in absence of zinc, for the GBD monomer.

(E) Superimposition of the structure of the 8-9F$_I$ Fn fragment (with 8F$_I$ and 9F$_I$ colored in orange and yellow, respectively) bound to a collagen peptide (green) onto the 7-8-9F$_I$ superdomain (same color code as Figure 1B).

homodimer formation. Remarkably, four Zn^{2+} ion binding sites are made by residues from both protomers and as a consequence are involved in dimer formation (Figure 2C). Two are located at the interface between 2F$_{II}$ and the C-ter lobe, and their coordination spheres are made by Asp^{522} and His^{539} from one monomer and His^{383} from the second (Figure S2C). The two remaining Zn^{2+} ions are bound between 1F$_{II}$ and the C-ter lobes. They are chelated by His^{404} and Asp^{433} from one protomer and His^{466} and Glu^{468} from the second (Figure S2D). Analysis of the electrostatic surface potential of the GBD monomer reveals that these four Zn^{2+} ions are spread over highly negatively charged patches (Figure 2D). Partial neutralization of these electrostatic surfaces may also be a crucial factor for dimer formation (Figure 2B). Zn-binding residues are very well conserved among mammal Fn sequences. Full details and sequence alignment of Zn sites are provided in Supplemental Experimental Procedures.

To strengthen our crystallographic observations, the quaternary structure of Fn-GBD was studied in solution. Sedimentation equilibrium experiments were performed by analytical ultracentrifugation. Absorbance scans were acquired three times at five speeds with GBD samples at 0.035, 0.16, and 1 mg/ml in either $ZnSO_4$ or EDTA conditions. All 15 scans acquired at 1 mg/ml in the presence of Zn^{2+} fit better with a dimer (Figure 3A; Figure S4) (MW = 84,281 Da), whereas in the presence of EDTA (or other divalent cations such as Mg^{2+} or Ca^{2+}), a monomer model gave the best fit (Figure 3B; Figure S5) (MW = 42,145 Da compared with 42,436 Da as measured by MALDI-TOF mass spectrometry, respectively). We analyzed monomer-dimer equilibrium during a sedimentation velocity experiment using GBD samples at 0.16 mg/ml in either presence or absence of Zn^{2+}. Absorbance scans were analyzed using a continuous distribution of sedimentation coefficients c(s). Figure 3C displays the analysis of a scan for two species interpreted as the monomer (s = 3.77S) and the dimer (s = 6.00S) in the presence of Zn^{2+}. Data fitting with a ratio f/f_0 = 1.20 (molecular axis ratio a/b = 2.3) and a fixed meniscus position provided estimation of the MW of 42,440 and 84,860 Da for the monomer and the dimer species, respectively. In the absence of Zn^{2+}, the coefficient velocity is lower (s = 2.95 S) and the ratio f/f_0 as to be set to 1.75 to keep a good fit corresponding to a MW of 42,810 Da. The dimerization equilibrium constant could not be properly measured because of monomer aggregation, but from the sedimentation velocity fit we estimated a dissociation constant of about 4.7 μM. Altogether, these data show that in the absence of Zn^{2+}, the GBD molecule is monomeric, whereas at 5 mM $ZnSO_4$, it is present as a mixture of both monomers and homodimers. In addition, the sedimentation coefficient of the monomer increases proportionally with $ZnSO_4$ concentration, suggesting that Zn^{2+} induces compaction of the GBD monomer (see Figure S4 and Supplemental Experimental Procedures for details). A possible scenario is that Zn^{2+} causes structural rearrangements within 8F$_I$, leading to formation of the superdomain, compaction of the monomeric form, and finally to dimer formation.

Although fibronectin was shown to exist in multiple oligomeric states in response to the physicochemical properties of the solution and the physiological interactions with other protein partners in the extracellular matrix (Aguirre et al., 1994; Erickson and Carrell, 1983; Morla et al., 1994), little is known about these states at the structural level. Intact Fn exists as a dimer due to the presence of two disulfide bonds at the C-terminal region, but other regions (the 70-kDa N-terminal and 1F$_{III}$–6F$_{III}$ fragments) were proposed to be involved in dimer formation (Aguirre et al., 1994; Vakonakis et al., 2007). However, all available detailed structural information on modules and combinations of modules have only revealed the presence of monomeric species so far. The present Fn-GBD structure is the first example of a dimeric form of an Fn fragment.

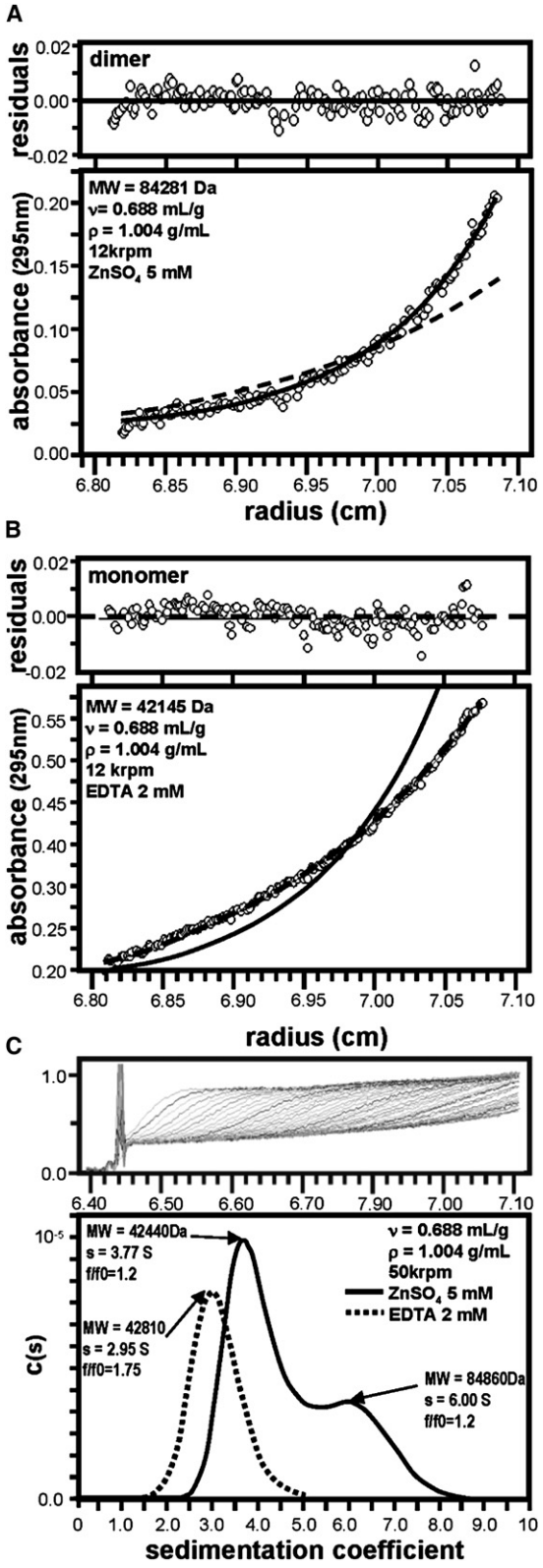

Figure 3. Effect of Zn^{2+} Ions on GBD Quaternary Structure

(A and B) Sedimentation equilibrium of GBD at a concentration of 1 mg/ml in either 5 mM $ZnSO_4$ (A) or 2 mM EDTA (B). A representative absorbance scan at 12 krpm is shown out of the 15 scans used for the fitting (three repeated scans acquired at five speeds). Calculated curves are drawn for the dimer as a solid line and for the monomer as a dashed line. Residuals for the best fit are indicated in the upper panel. Parameters used for the fit are indicated. Corresponding MW are reported for the best fit.

(C) Sedimentation velocity experiments performed with GBD at a concentration of 0.16 mg/ml. The data presented in the top panel for GBD in EDTA (absorbance versus radius) were analyzed according to the continuous c(*s*) analysis method. Parameters used for the fit are indicated. Sedimentation coefficients are reported for every peaks as well as their corresponding MW and friction ratio f/f_0.

Collagen/Gelatin Binding

Collagen assembly is spatially and temporally integrated with fibronectin polymerization in vascular smooth muscle cells (Li et al., 2003). Collagen and fibronectin specifically interact in the extracellular matrix. The quaternary structure of Fn-GBD is therefore clearly relevant to understand its interactions with collagen. The interaction between Fn-GBD and collagen has mainly been studied in vitro using gelatin (Engvall and Ruoslahti, 1977). Various module pairs ($6F_I$-$1F_{II}$, $2F_{II}$-$7F_I$, and $8F_I$-$9F_I$) obtained by either proteolysis of Fn-GBD or overexpression of recombinant constructs were all shown to bind to gelatin albeit with lower activity compared with intact Fn-GBD.

Gelatin-binding studies with fragments of GBD showed that all six modules are required for full activity, suggesting cooperativity between these six modules (Ingham et al., 1989; Katagiri et al., 2003). The very compact Fn-GBD structure shows that its modules strongly interact, in line with the fact that they all seem required for full gelatin affinity. The migration stimulating factor (MSF), an isoform obtained by alternative splicing of the Fn mRNA, corresponds to the 70-kD N-terminal fragment and encompasses the Fn-GBD. The secretion of this protein increases migration into 3D type-I collagen gels of fetal fibroblasts compared with adult cells (Schor et al., 1985). The Ile-Gly-Asp triplets (IGD) from $7F_I$ and $9F_I$ have been shown to be crucial for MSF motogenic activity (Millard et al., 2007; Schor et al., 2003). Erat et al. (2009) recently showed that Fn-GBD specifically binds to a type-I collagen peptide adjacent to the MMP1 cleavage site, spanning residues G788–G799, with a binding constant of 5 μM (Erat et al., 2009). The $8F_I$-$9F_I$ fragment binds this peptide with the same affinity as the complete Fn-GBD. The crystal structure of the α1 G788–G799 peptide in complex with $8F_I$-$9F_I$ showed that both F_I modules adopt the canonical F_I fold. The collagen peptide forms a β-strand running antiparallel to strand E from $8F_I$, in a manner reminiscent of the mode of interaction previously observed in complexes between proteins from pathogenic bacteria and F_I modules (Schwarz-Linek et al., 2003). We superposed the sheet formed by strands C to E in the $8F_I$ bound to α1 G788–G799 peptide onto that of the $8F_I$ as observed in our crystal structure. Strand E from $8F_I$ that runs antiparallel to the collagen peptide is accessible in the $7F_I$-$8F_I$-$9F_I$ superdomain (Figure 2E). We investigated whether the collagen peptide would be able to maintain its interaction with strand E in the GBD through modeling. We were able to position part of the G788–G799 peptide in our GBD antiparallel to the E strand with a similar configuration as observed for the 8-$9F_I$ collagen peptide complex. In the latter complex, the collagen peptide also interacts with $9F_I$. However, the 9 F_I module in the GBD is differently oriented relative to $8F_I$ so that interactions between the collagen peptide and $9F_I$ cannot

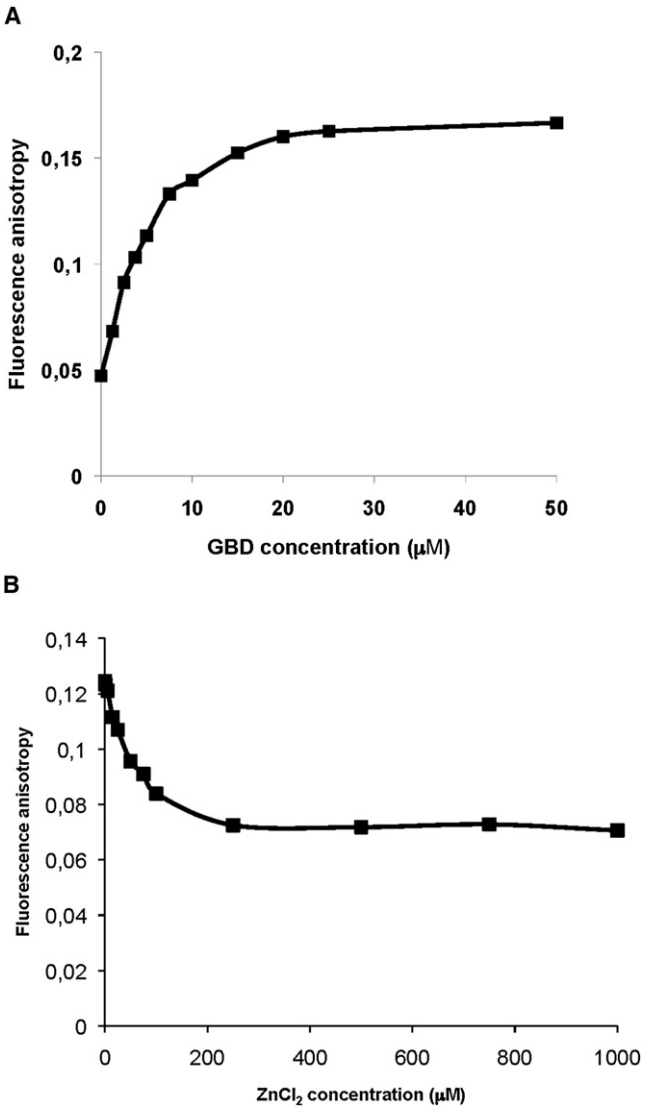

Figure 4. Effect of Zinc on GBD Affinity for Collagen

(A) Fluorescence anisotropy titration of collagen peptide by GBD.

(B) Fluorescence anisotropy titration of collagen peptide incubated with 25 μM GBD with increasing concentrations of $ZnCl_2$.

be maintained in the GBD upon the rearrangement induced by zinc.

From these observations, we tested whether Zn affects the binding affinity of GBD for collagen peptide. We used fluorescence anisotropy titrations of a fluorescently labeled high-affinity collagen peptide [α_1(I) G_{778}–G_{799}] with GBD. In absence of Zn, we obtained a dissociation constant of 5 μM, in agreement with the value obtained by Erat et al. (2009) (Figure 4A). To investigate the effect of Zn, we incubated the fluorescently labeled α_1(I) G_{778}–G_{799} peptide with excess GBD (25 μM) and then titrated with increasing amounts of $ZnCl_2$. As can be seen from Figure 4B, the anisotropy of the peptide fluorescence decreases with increasing $ZnCl_2$ concentrations and finally reaches a stable value at 200 μM $ZnCl_2$. Because $ZnCl_2$ has no effect on the anisotropy of the peptide alone (data not shown), we conclude that the addition of $ZnCl_2$ dissociates the collagen peptide from the GBD. Direct titration of the peptide with GBD in the presence of 3 mM $ZnCl_2$ did not reveal any binding (data not shown). We conclude that although potential collagen-binding sites remain accessible, the structural rearrangements and dimer formation induced by Zn inhibit the binding of a high-affinity collagen peptide.

DISCUSSION

A number of solution and crystal structures of Fn fragments are now available, but we are still far from a molecular picture of its dynamics and interactions with its partners in the extracellular matrix. Fn is a flexible protein whose conformation and association state depend on the physicochemical and physiological properties of its environment. The conformation of plasma Fn is dependent upon the pH and ionic strength of the solution. It expands from a compact conformation (at physiological pH and at lower ionic strength) to an extended conformation (at increased pH or salt concentration) without any significant changes in secondary or tertiary structure (Erickson and Carrell, 1983; Johnson et al., 1999; Rocco et al., 1987). It is believed that this expansion is related to the flexibility in the links between some domains. Sedimentation experiments suggested that an interaction between $2F_{III}$-$3F_{III}$ and $13F_{III}$-$14F_{III}$ is responsible for the compact form (Johnson et al., 1999). The assembly of Fn fibers is a complex and stepwise process. Fn is converted from a secreted compact globular dimer, incapable of fibril assembly (Erickson and Carrell, 1983; Johnson et al., 1999), into a dense network of interconnected fibrils in response to binding to the cell receptor integrins. It was proposed that the combination of interaction of Fn with itself, with integrins or other proteins from the ECM and mechanical tension unmasks cryptic assembly sites along the Fn chain. The most important Fn self-binding sites seem to be located in the N terminus (Vakonakis et al., 2007).

Fn-GBD adopts a complex compact dimer that could not be predicted from structures of its individual modules. The Fn-GBD structure reveals many surprising features. First, GBD binds a number of well-defined Zn^{2+} ions that drastically influence its tertiary and quaternary organization. Zn clearly plays a role in the structural rearrangement of $8F_I$, which is involved in multiple Zn^{2+} binding sites (Figure 1D; Figure S2). The noncanonical $8F_I$ fold is further stabilized by (*i*) extensive β sheet formation with the neighboring F_Is (especially the extensive β-sheet formation between strand E from $7F_I$ and strand C from $8F_I$) and (*ii*) dimer packing of the common β-sheet onto $1F_{II}$. Ultracentrifugation solution measurements further suggest that at lower concentrations, Zn binding compacts GBD, and at higher concentrations leads to dimer formation. We propose that this compaction is due to the association of $7F_I$-$8F_I$-$9F_I$ into a single domain that tightly interacts with $1F_{II}$. The $7F_I$-$8F_I$-$9F_I$ part also contributes the main GBD dimer interaction surface. Zn therefore affects the secondary, tertiary, and quaternary structures of Fn-GBD, and the effects are coupled.

We ignore for the moment whether Zn binding to Fn is physiological. Obviously, Zn concentrations needed for crystal formation are very high, but Zn could exert functional effects at much lower concentrations in vivo. We showed that binding to a high-affinity collagen peptide is inhibited at submillimolar

Zn concentrations. We therefore hypothesize that Zn binding could exert a possible regulatory role on the physiological behavior of fibronectin. Zn concentrations in biological samples depend much on type of tissue. Reported values in serum and whole blood are between 15 and 100 μM, but rise to millimolar levels in liver and hair (Iyengar and Woittiez, 1988).

Interestingly, a MSF double-mutant where two Zn^{2+} chelating histidine residues (His^{535} and His^{539}) were substituted by phenylalanine displays a decreased cell migratory activity compared with the wild type (Houard et al., 2005). F_I modules are extremely robust as exemplified by stability measurements on $6F_I$, $7F_I$, and $9F_I$ (Tm around 60°C measurable only in the presence of 6 M guanidinium chloride (Litvinovich et al., 1991). Surprisingly, the $8F_I$ module has a much weaker thermostability (Tm around 65°C without requirement for guanidinium chloride), which could be related to its capacity to undergo large conformational changes.

Bivalent metal ions are known to play an important role in the regulation of extracellular signaling proteins. For instance, calcium-mediated homodimer formation is well documented for cadherins, cell adhesion proteins involved in embryonic morphogenesis and stable cell-cell interactions (Takeichi, 1990). Many ECM proteins (MMPs that use Zn^{2+} as an activating metal, but also decorin, biglycan, laminin, nidogen, and others) exhibit high affinity for zinc. Reports in the literature on the effect of zinc on the structure or function of Fn are sparse. However, a study has already described that the GBD can be retained on a zinc-charged column (Gmeiner et al., 1995) and more recently the alternatively spliced type-III connecting segment (IIICS) located between $14F_{III}$ and $15F_{III}$ modules, has been shown to bind one zinc ion (Askari et al., 2007). In addition, a low zinc-dependent gelatinase activity has been associated with Fn and particularly to its GBD fragment (Boudjennah et al., 1998; Houard et al., 2005; Lambert Vidmar et al., 1991; Schnepel and Tschesche, 2000). Site-directed mutagenesis experiments have identified His^{535} and His^{539} from the HEXXH motif present in $8F_I$ module to be important for this activity. In our structure, these two residues are involved in zinc ion binding (Figure S2C), but no structural homology is observed with metalloproteases.

Our findings very clearly show that zinc has a dramatic effect on the structure and organization of Fn-GBD. It remains an open question whether zinc has any role in the cellular behavior of Fn. The role of Zn^{2+} for the biological function, dynamics, and structure of both fibronectin and MSF should be further investigated.

EXPERIMENTAL PROCEDURES

Crystallization and Structure Solution

The 45-kDa gelatin-binding domain (GBD) purchased as a lyophilized product from Sigma was generated by successive digestion of human fibronectin by cathepsin D and trypsin. It was resuspended in 50 mM Tris/HCl (pH 7.4) and 150 mM NaCl. Lens-shaped crystals (100 μm) could only be obtained by mixing 0.1 μl of protein solution (30 mg/ml) with an equal volume of crystallization solution [25–30% PEG 550 MME, 0.1 M MES (pH 6.5), 30–50 mM $ZnSO_4$]. Attempts to grow larger crystals failed due to protein precipitation when mixing larger volumes of protein and crystallization solution. Prior to data collection, crystals were directly flash-frozen in liquid nitrogen without addition of any cryoprotectant. The 3-Å resolution SAD data at the Zn edge and the 2.4-Å native data could be recorded on beamline ID23-EH1 (European Synchrotron Radiation Facility, Grenoble, France). The structure was determined by the SAD method (single wavelength anomalous dispersion) using the anomalous signal from bound Zn^{2+} ions. Data were processed using the XDS package (Kabsch, 1993). The space group was $P3_221$ with one molecule per asymmetric unit. Seven zinc atom sites were found with the program SHELXD in the 50-4 Å resolution range (Schneider and Sheldrick, 2002). Refinement of the Zn^{2+} ion coordinates and occupancy, phasing, and density modification were performed with the program SHARP (Bricogne et al., 2003). The quality of the final phases allowed automatic building of a partial model with the program RESOLVE (Terwilliger, 1999). This model was completed by iterative cycles of manual rebuilding using the "TURBO" molecular modeling program (http://www.afmb.univ-mrs.fr/-TURBO-) followed by refinement with the BUSTER-TNT program (Blanc et al., 2004).

Residues Gln^{297} to Cys^{545} and Trp^{533} to Thr^{604} are well defined in electron density and fall within the allowed regions of the Ramachandran plot as defined by the program PROCHECK. Electron density allowed to model two N-acetyl-glucosamine (NAG) bound to Asn^{430}, one to Asn^{528}, and one to Asn^{542}. In addition, 61 water molecules, two portions of PEG 550 MME used as crystallization agent, and seven Zn^{2+} ions have been built. Statistics for all the data collections and refinement are summarized in Table S1.

Analysis of the Oligomerization State of GBD in the Presence of Zn^{2+}

The oligomerization state of GBD was studied by sedimentation-diffusion equilibrium experiments using an Optima XL-I analytical ultracentrifuge (Beckman-Coulter). Six aluminum two-sector cells were loaded with 150 μl of GBD samples in 20 mM Tris-HCl (pH 7.5), 150 mM NaCl at three concentrations (0.035, 0.16, and 1 mg/ml) in the presence of either 5 mM $ZnSO_4$ or 2 mM EDTA. These cells were centrifuged using an eight-hole AN50-titane rotor until the sedimentation-diffusion equilibrium was reached (18 hr at 20°C) at each of five speeds performed: 9, 10, 11, 12, and 14 krpm. Three absorbance scans were recorded at the optimal wavelengths of 230, 280, or 295 nm, respectively, for each speed and corresponding sample concentration. The contributions of GBD at the sample meniscus toward the center of the rotor were measured from an average of three absorbance scans at 50 krpm to set up the absorbance offsets. The sedimentation equilibrium data for GBD were fitted on models, first using Equation 1 describing a single ideal species:

$$A_r = A_{r_0} e^{\left[(M(1-v\rho)\omega^2/2RT)(r^2-r_0^2)\right]}, \quad (1)$$

then Equation 2 considering a self-associating species:

$$A_r = A_{r_0} e^{\left[(M(1-v\rho)\omega^2/2RT)(r^2-r_0^2)\right]} + A_{n-mer,r_0} e^{\left[(nM(1-v\rho)\omega^2/2RT)(r^2-r_0^2)\right]} \quad (2)$$

where the absorbance A_r at any radial position r, is related to the molecular weight, M; R is the gas constant, T is the temperature in Kelvin, ν is the partial specific volume of the molecule, and ρ is the buffer density. A partial specific volume ν of 0.688 ml/g was calculated for GBD from the amino-acid composition (0.692 ml/g) and the carbohydrate composition (0.660 ml/g), according to their respective contribution to the total weight. Solvent density $\rho = 1.004$ g/ml was set from tables. A_{r0} is the absorbance at a radial reference distance, r_0, ω is the angular velocity, and n is the number of identical subunits of molecular weight M within the n-mer. The 15 absorbance scans (three scans per speed for five speeds) per each GBD concentration were fitted simultaneously to the model equations by using the software Origin 6.0 (Microcal). Models were selected from the lowest variance values and the unbiased residual value distributions.

The sedimentation coefficient of GBD was determined from sedimentation velocity experiments performed using the analytical ultracentrifuge at a rotor speed of 50 krpm and at 20°C in two aluminum two-sector cells using a four-hole AN60-titane rotor. One concentration (0.16 mg/ml) in 20 mM Tris-HCl (pH 7.5), 150 mM NaCl was analyzed in the presence of either 5 mM $ZnSO_4$ or 2 mM EDTA. A total of 120 absorbance and refractive index scans were acquired for both samples with Raleigh interference optics every 150 s. The data were analyzed according to the continuous c(s) analysis method smoothed with a maximum entropy regularization using Sedfit 94 (Dam and Schuck, 2004). This method deconvolutes the effects of diffusion broadening, yielding high-resolution sedimentation coefficient (s) distribution.

Fluorescence Anisotropy Experiments

Fluorescence anisotropy measurements were performed at 25°C in a 20 mM Tris-Cl (pH 7.4), 150 mM NaCl buffer by using a Varian Cary Eclipse

Fluorescence Spectrophotometer. Samples of 75-nM FITC-labeled collagen peptide α_1(I) G_{778}–G_{799} (generous gift from I. Vakonakis, Oxford University, UK) titrated with increasing concentrations of protein or $ZnCl_2$ were excited at 485 nm with a 10-nm cutoff, and fluorescence was observed at 525 nm. Experiments were performed in duplicate.

ACCESSION NUMBERS

The atomic coordinates and structure factors have been deposited in the Protein Data Bank, www.pdb.org (PDB ID code 3M7P).

SUPPLEMENTAL INFORMATION

Supplemental Information include five figures and Supplemental Experimental Procedures and can be found with this article online at doi:10.1016/j.str.2010.03.012.

ACKNOWLEDGMENTS

We are indebted to N. Ulryck for their technical assistance with GBD crystallization and B. Faivre for fluorescence measurements. We thank I. Vakonakis for the generous gift of the fluorescently labeled collagen peptides used in this study. We acknowledge K. Blondeau, D. Liger, X. Houard, and V. Dive for fruitful discussion. This work was supported by the European Commission as part of SPINE2-Complexes (LSHG-CT-2006-031220) project and by a grant from the Association pour la Recherche sur le Cancer (ARC no. 4966).

Received: February 10, 2010
Revised: March 19, 2010
Accepted: March 20, 2010
Published: June 8, 2010

REFERENCES

Aguirre, K.M., McCormick, R.J., and Schwarzbauer, J.E. (1994). Fibronectin self-association is mediated by complementary sites within the amino-terminal one-third of the molecule. J. Biol. Chem. *269*, 27863–27868.

Askari, J.A., Thornton, D.J., Humphries, J.D., Buckley, P.A., and Humphries, M.J. (2007). The alternatively spliced type III connecting segment of fibronectin is a zinc-binding module. Matrix Biol. *26*, 485–493.

Baron, M., Norman, D., Willis, A., and Campbell, I.D. (1990). Structure of the fibronectin type 1 module. Nature *345*, 642–646.

Blanc, E., Roversi, P., Vonrhein, C., Flensburg, C., Lea, S.M., and Bricogne, G. (2004). Refinement of severely incomplete structures with maximum likelihood in BUSTER-TNT. Acta Crystallogr. D Biol. Crystallogr. *60*, 2210–2221.

Bocquier, A.A., Potts, J.R., Pickford, A.R., and Campbell, I.D. (1999). Solution structure of a pair of modules from the gelatin-binding domain of fibronectin. Structure *7*, 1451–1460.

Boudjennah, L., Dalet-Fumeron, V., and Pagano, M. (1998). Expression of collagenase/gelatinase activity from basement-membrane fibronectin—isolation after limited proteolysis of a bovine lens capsule and molecular definition of this thiol-dependent zinc metalloproteinase. Eur. J. Biochem. *255*, 246–254.

Bricogne, G., Vonrhein, C., Flensburg, C., Schiltz, M., and Paciorek, W. (2003). Generation, representation and flow of phase information in structure determination: recent developments in and around SHARP 2.0. Acta Crystallogr. D Biol. Crystallogr. *59*, 2023–2030.

Chothia, C., and Jones, E.Y. (1997). The molecular structure of cell adhesion molecules. Annu. Rev. Biochem. *66*, 823–862.

Dam, J., and Schuck, P. (2004). Calculating sedimentation coefficient distributions by direct modeling of sedimentation velocity concentration profiles. Methods Enzymol. *384*, 185–212.

Engvall, E., and Ruoslahti, E. (1977). Binding of soluble form of fibroblast surface protein, fibronectin, to collagen. Int. J. Cancer *20*, 1–5.

Erat, M.C., Slatter, D.A., Lowe, E.D., Millard, C.J., Farndale, R.W., Campbell, I.D., and Vakonakis, I. (2009). Identification and structural analysis of type I collagen sites in complex with fibronectin fragments. Proc. Natl. Acad. Sci. USA *106*, 4195–4200.

Erickson, H.P., and Carrell, N.A. (1983). Fibronectin in extended and compact conformations. Electron microscopy and sedimentation analysis. J. Biol. Chem. *258*, 14539–14544.

Erickson, H.P., Carrell, N., and McDonagh, J. (1981). Fibronectin molecule visualized in electron microscopy: a long, thin, flexible strand. J. Cell Biol. *91*, 673–678.

Gmeiner, B., Leibl, H., Zerlauth, G., and Seelos, C. (1995). Affinity binding of distinct functional fibronectin domains to immobilized metal chelates. Arch. Biochem. Biophys. *321*, 40–42.

Houard, X., Germain, S., Gervais, M., Michaud, A., van den Brûle, F., Foidart, J.M., Noël, A., Monnot, C., and Corvol, P. (2005). Migration-stimulating factor displays HEXXH-dependent catalytic activity important for promoting tumor cell migration. Int. J. Cancer *116*, 378–384.

Hynes, R.O. (1990). Fibronectins (New York: Springer-Verlag).

Ingham, K.C., Brew, S.A., and Isaacs, B.S. (1988). Interaction of fibronectin and its gelatin-binding domains with fluorescent-labeled chains of type I collagen. J. Biol. Chem. *263*, 4624–4628.

Ingham, K.C., Brew, S.A., and Migliorini, M.M. (1989). Further localization of the gelatin-binding determinants within fibronectin. Active fragments devoid of type II homologous repeat modules. J. Biol. Chem. *264*, 16977–16980.

Ingham, K.C., Brew, S.A., and Novokhatny, V.V. (1995). Influence of carbohydrate on structure, stability, and function of gelatin-binding fragments of fibronectin. Arch. Biochem. Biophys. *316*, 235–240.

Ingham, K.C., Brew, S.A., and Migliorini, M. (2002). Type I collagen contains at least 14 cryptic fibronectin binding sites of similar affinity. Arch. Biochem. Biophys. *407*, 217–223.

Iyengar, V., and Woittiez, J. (1988). Trace elements in human clinical specimens: evaluation of literature data to identify reference values. Clin. Chem. *34*, 474–481.

Johnson, K.J., Sage, H., Briscoe, G., and Erickson, H.P. (1999). The compact conformation of fibronectin is determined by intramolecular ionic interactions. J. Biol. Chem. *274*, 15473–15479.

Kabsch, W. (1993). Automatic processing of rotation diffraction data from crystals of initially unknown symmetry and cell constants. J. Appl. Cryst. *26*, 795–800.

Katagiri, Y., Brew, S.A., and Ingham, K.C. (2003). All six modules of the gelatin-binding domain of fibronectin are required for full affinity. J. Biol. Chem. *278*, 11897–11902.

Kleinman, H.K., McGoodwin, E.B., Martin, G.R., Klebe, R.J., Fietzek, P.P., and Woolley, D.E. (1978). Localization of the binding site for cell attachment in the alpha1(I) chain of collagen. J. Biol. Chem. *253*, 5642–5646.

Lambert Vidmar, S., Lottspeich, F., Emod, I., Imhoff, J.M., and Keil-Dlouha, V. (1991). Collagen-binding domain of human plasma fibronectin contains a latent type-IV collagenase. Eur. J. Biochem. *201*, 79–84.

Leahy, D.J., Aukhil, I., and Erickson, H.P. (1996). 2.0 A crystal structure of a four-domain segment of human fibronectin encompassing the RGD loop and synergy region. Cell *84*, 155–164.

Li, S., Van Den Diepstraten, C., D'Souza, S.J., Chan, B.M., and Pickering, J.G. (2003). Vascular smooth muscle cells orchestrate the assembly of type I collagen via alpha2beta1 integrin, RhoA, and fibronectin polymerization. Am. J. Pathol. *163*, 1045–1056.

Litvinovich, S.V., Strickland, D.K., Medved, L.V., and Ingham, K.C. (1991). Domain structure and interactions of the type I and type II modules in the gelatin-binding region of fibronectin. All six modules are independently folded. J. Mol. Biol. *217*, 563–575.

Liu, X., Zhao, Q., and Collodi, P. (2003). A truncated form of fibronectin is expressed in fish and mammals. Matrix Biol. *22*, 393–396.

McDonald, J.A., Kelley, D.G., and Broekelmann, T.J. (1982). Role of fibronectin in collagen deposition: Fab′ to the gelatin-binding domain of fibronectin

inhibits both fibronectin and collagen organization in fibroblast extracellular matrix. J. Cell Biol. *92*, 485–492.

Millard, C.J., Ellis, I.R., Pickford, A.R., Schor, A.M., Schor, S.L., and Campbell, I.D. (2007). The role of the fibronectin IGD motif in stimulating fibroblast migration. J. Biol. Chem. *282*, 35530–35535.

Morla, A., Zhang, Z., and Ruoslahti, E. (1994). Superfibronectin is a functionally distinct form of fibronectin. Nature *367*, 193–196.

Pankov, R., and Yamada, K.M. (2002). Fibronectin at a glance. J. Cell Sci. *115*, 3861–3863.

Pickford, A.R., Smith, S.P., Staunton, D., Boyd, J., and Campbell, I.D. (2001). The hairpin structure of the (6)F1(1)F2(2)F2 fragment from human fibronectin enhances gelatin binding. EMBO J. *20*, 1519–1529.

Potts, J.R., and Campbell, I.D. (1996). Structure and function of fibronectin modules. Matrix Biol. *15*, 313–320, discussion 321.

Potts, J.R., Bright, J.R., Bolton, D., Pickford, A.R., and Campbell, I.D. (1999). Solution structure of the N-terminal F1 module pair from human fibronectin. Biochemistry *38*, 8304–8312.

Rocco, M., Infusini, E., Daga, M.G., Gogioso, L., and Cuniberti, C. (1987). Models of fibronectin. EMBO J. *6*, 2343–2349.

Rudiño-Piñera, E., Ravelli, R.B., Sheldrick, G.M., Nanao, M.H., Korostelev, V.V., Werner, J.M., Schwarz-Linek, U., Potts, J.R., and Garman, E.F. (2007). The solution and crystal structures of a module pair from the Staphylococcus aureus-binding site of human fibronectin—a tale with a twist. J. Mol. Biol. *368*, 833–844.

Schneider, T.R., and Sheldrick, G.M. (2002). Substructure solution with SHELXD. Acta Crystallogr. D Biol. Crystallogr. *58*, 1772–1779.

Schnepel, J., and Tschesche, H. (2000). The proteolytic activity of the recombinant cryptic human fibronectin type IV collagenase from E. coli expression. J. Protein Chem. *19*, 685–692.

Schor, S.L., Schor, A.M., Rushton, G., and Smith, L. (1985). Adult, foetal and transformed fibroblasts display different migratory phenotypes on collagen gels: evidence for an isoformic transition during foetal development. J. Cell Sci. *73*, 221–234.

Schor, S.L., Schor, A.M., Grey, A.M., and Rushton, G. (1988). Foetal and cancer patient fibroblasts produce an autocrine migration-stimulating factor not made by normal adult cells. J. Cell Sci. *90*, 391–399.

Schor, S.L., Ellis, I.R., Jones, S.J., Baillie, R., Seneviratne, K., Clausen, J., Motegi, K., Vojtesek, B., Kankova, K., Furrie, E., et al. (2003). Migration-stimulating factor: a genetically truncated onco-fetal fibronectin isoform expressed by carcinoma and tumor-associated stromal cells. Cancer Res. *63*, 8827–8836.

Schwarz-Linek, U., Werner, J.M., Pickford, A.R., Gurusiddappa, S., Kim, J.H., Pilka, E.S., Briggs, J.A., Gough, T.S., Höök, M., Campbell, I.D., and Potts, J.R. (2003). Pathogenic bacteria attach to human fibronectin through a tandem beta-zipper. Nature *423*, 177–181.

Sharma, A., Askari, J.A., Humphries, M.J., Jones, E.Y., and Stuart, D.I. (1999). Crystal structure of a heparin- and integrin-binding segment of human fibronectin. EMBO J. *18*, 1468–1479.

Takeichi, M. (1990). Cadherins: a molecular family important in selective cell-cell adhesion. Annu. Rev. Biochem. *59*, 237–252.

Terwilliger, T.C. (1999). Reciprocal-space solvent flattening. Acta Crystallogr. D Biol. Crystallogr. *55*, 1863–1871.

Vakonakis, I., Staunton, D., Rooney, L.M., and Campbell, I.D. (2007). Interdomain association in fibronectin: insight into cryptic sites and fibrillogenesis. EMBO J. *26*, 2575–2583.

Williams, M.J., Phan, I., Harvey, T.S., Rostagno, A., Gold, L.I., and Campbell, I.D. (1994). Solution structure of a pair of fibronectin type 1 modules with fibrin binding activity. J. Mol. Biol. *235*, 1302–1311.

